Research Article

Sang-Lae Lee*

Active vibration suppression of wind turbine blades integrated with piezoelectric sensors

Abstract: As the wind turbine size gets larger, the optimal design of blades, which is a major source of energy for the wind turbines and also the cause of loads, is becoming more important than anything else. Therefore, reducing the load on the blade should be the top priority in designing a blade. In this article, we studied the vibration control of the stiffened wind blades subjected to a wind load with piezoelectric sensors and actuators to mitigate fluctuations in loading and adding damping to the blade. The model is a laminated composite blade with a shear web and the PZT piezomaterial layers embedded on the top and bottom surfaces act as a sensor and actuator, respectively. A uniformly distributed external wind load is assumed over the entire plate surface for simplicity. The first-order shear deformation (FSDT) theory is adopted, and Hamilton's principle is used to derive the finite element equation of motion. The modal superposition technique and the Newmark-β method are used in numerical analysis to calculate the dynamic response. Using the constant gain negative velocity feedback control algorithm, vibration characteristics and transient responses are compared. Furthermore, vibration control at various locations of the shear webs subjected to an external load is discussed in detail. Through various calculation results performed in this study, this article proposes a method of designing a blade that can reduce the load by actively responding to the external load acting on the wind turbine blade.

Keywords: vibration suppression, shear web, piezoelectric, active control, mitigating fluctuations, reducing loads

---
* **Corresponding author: Sang-Lae Lee,** Korean Register of Shipping (KR), R&D Division, System Safety Team, Busan, 46762, Republic of Korea, e-mail: sllee@krs.co.kr

Nomenclature

$\boldsymbol{\delta}_p^e$	element nodal displacement vector of a plate
$\boldsymbol{\delta}_{xs}^e$	element nodal displacement vector of x-shear web
t_a	thickness of the piezoelectric actuator layer
$\boldsymbol{F}_p$	resultant force of a plate
$\boldsymbol{M}_p$	resultant moment of a plate
ϕ_a	actuating voltage
F_{xs}	resultant axial stress of the x-shear web
M_{xs}	resultant bending stress of the x-shear web
V_{xs}	resultant shear stress of the x-shear web
$\boldsymbol{\eta}$	modal displacement vector
$\boldsymbol{\xi}$	state-space variable
$\boldsymbol{\Phi}$	modal matrix with n retained modes
$\boldsymbol{A}_{st}$	system matrix in a state-space form
$\boldsymbol{B}_{st}$	control matrix in a state-space form
$\boldsymbol{U}_f$	disturbance matrix in a state-space form
μ	shear-web location parameter
p	plate element
xs	x-shear-web element
ys	y-shear-web element

1 Introduction

A wind turbine blade is a complex engineering system, subjected to highly fluctuating and irregular loads. These vibrations can cause catastrophic damages due to structural fatigue and progressive failure of the lightweight structure, resulting in unexpected maintenances, reduced efficiency and shortened lifetime. To improve the reliability of such lightweight structures, several techniques were used, both experimentally and numerically, to either limit or change the vibration responses of such systems. With the recent developments in the sensor–actuator technologies and in smart materials, especially piezoelectric materials, an active vibration control has been utilized for vibration suppression. The piezoelectric sensors are used to detect and quantify the mechanical stress applied to the materials. This is due to the direct piezoelectric

effect, wherein the material generates a certain amount of electric charge when subjected to physical deformation. Actuators, on the other hand, operate in the opposite direction. Rather than generating electric charges, when given a certain amount of electrical energy, the material undergoes mechanical deformation due to the converse piezoelectric effect. These two flexible effects, coupled with the economic availability of the piezoelectric materials and the ease with which they can be bonded to other materials, make the popularity of piezoelectric materials well justified.

In past years, a number of issues related to nonlinear aero-elastic modeling and active vibration control based on piezoelectric actuation were investigated. The vibration control of a thin-walled beam integrated with piezoelectric fiber composites and the modeling and nonlinear vibration analysis of anisotropic laminated cylindrical shells or plates with the piezoelectric fiber-reinforced composite actuators were analyzed [1–8]. St-Amant and Cheng [9] studied the simulations and experiments for the active vibration control of a plate with integrated piezoceramics. Balamurugan and Marayanan [10] investigated the mechanics and the coupled analysis of the piezo-laminated plate and curvilinear shell structures and their vibration control performance. Mukherjee et al. [11] studied the active vibration control of stiffened plates using piezoelectric effects. Based on the finite element method, Sadek and Tawfik [12] developed a refined higher-order displacement model for the analysis of concentrically and eccentrically stiffened laminated plates. The aerothermoelastic characteristics of a supersonic laminated cylindrical shell and the active flutter control of the aeroelastic structure using piezoelectric materials were analyzed by Song and Li [13]. Shen and Yang [14] dealt with small- and large-amplitude flexural vibrations of anisotropic shear-deformable laminated cylindrical shells with the piezoelectric fiber-reinforced composite actuators in thermal environments.

Meanwhile, many studies have been conducted on various types of beam models made of composite materials. Mirzaei et al. [15–17] investigated the functionally graded (FG) simple beam model using first-order shear deformation theory. Arefi and Zenkour [18,19] studied the transient analysis of a three-layer microbeam based on higher-order sinusoidal shear deformation theory. Kiani [20] studied the torsional vibration of FG carbon nanotube-reinforced conical shells. Jalaei and Civalek [21] examined the dynamic instability of the magnetically embedded viscoelastic porous FG nanobeam. Civalek et al. [22,23] dealt with the static stability and vibration analysis of microbeams.

In addition, various load-reduction studies using piezoelectric actuation were conducted in the wind blade field as well. Liu [24] investigated the classical flutter and flutter suppression of a composite wind blade beam composed of a single-cell thin-walled structure and an embedded piezoelectric patch. Using piezoelectric actuation on the wind blade, active control of classical flutter suppression was studied. Abdelrahman et al. [25] used an active vibration control method, numerically, for the vibration suppression of a wind turbine blade model, with a piezoelectric sensor and actuator. The effects of the piezoelectric size and the piezoelectric material properties on the vibration response were investigated. Hulskamp et al. [26] designed and constructed a scaled smart rotor, equipped with trailing-edge flaps, to study its fatigue load reduction potentials. The flaps were based on the piezoelectric thunder actuators, and the dynamic strain behavior of the blade was analyzed for the optimal placement of the sensors.

This article presents the investigation of the active vibration control of a stiffened laminated wind blade with piezoelectric materials under an external load. A study is conducted on how to reduce the load in an active way using a piezoelectric material when an external excessive load is applied to the wind turbine blade. This study provides a way for vibration suppression and active control of a wind turbine blade based on the piezoelectric actuation with an optimal shear-web location.

2 Stiffened laminated plate with piezoelectrics

The wind turbine blade is a load-carrying aerodynamic structure, which consists of suction and pressure aerodynamic shells, skin, spar cap and the shear webs, as shown in Figure 1. The skin requires the blade exterior to withstand the torsion load. Thus, it is a sandwich structure composed of bi-axle or tri-axle (2AX or 3AX) glass fibers and foam material. The foam material is used to enhance flexural stiffness and prevent buckling, and PVC foam or balsa wood is mainly used. Spar caps are inserted into the thick beams by stacking dozens of thin unidirectional fibers, which withstand most of the bending moment that occurs due to the wind load. The shear web is located between the skins. It has a sandwich structure consisting of bi-axle glass fiber and foam to withstand the transverse shear load. For the wind turbine blades, the spar cap enables the blade to be structurally
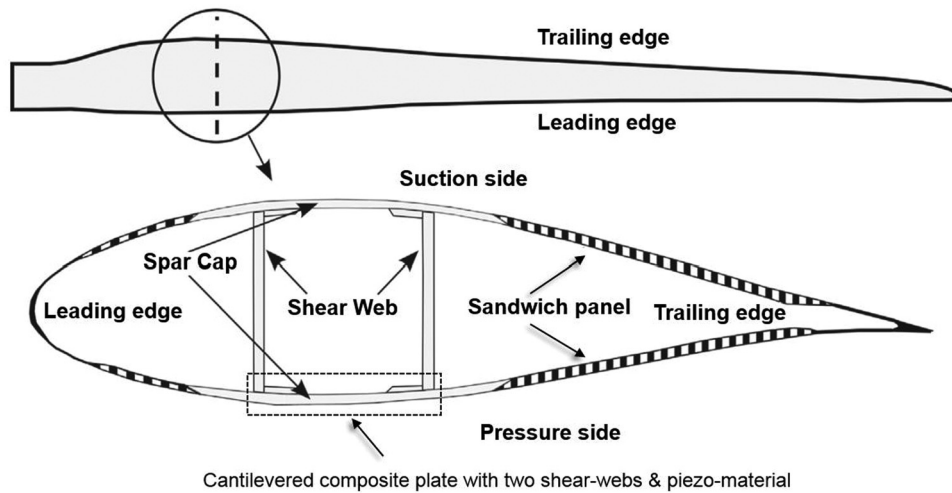
Figure 1: Cross-section of a wind turbine blade.

robust under a wind load. Additionally, the shear webs support the spar caps that play this role, and the positioning of the shear webs and the optimization of the spar caps are one of the most important factors in designing blades.

Considering these structural characteristics of the blade, a laminated composite plate, reinforced with a shear web in which a piezoelectric patch is embedded, which simplifies the spar cap area of the blades for various calculations, was used for this calculation, as shown in Figure 2. For various case studies and calculations, the wind turbine blade is replaced by a simplified rectangular model, composed of PZT piezo-material layers embedded on the top and bottom surfaces to act as a sensor and actuator, respectively. For simplicity, a uniform external load is assumed to be distributed over the entire plate

Figure 2: Cantilevered composite plate with two shear webs, piezoelectric sensors and actuators.

surfaces and the shear webs are assumed to be placed parallel to the geometric coordinates x.

2.1 Constitutive equations

Linear piezoelectric coupling for the kth layer between the elastic field and the electric field can be expressed by "direct" and "converse" piezoelectric equations, respectively.

The direct piezoelectric effect is given by

$$\boldsymbol{D}_k = \boldsymbol{e}_k \boldsymbol{\varepsilon}_k + \varepsilon_k \boldsymbol{E}_k, \tag{1}$$

whereas the converse piezoelectric effect is given by

$$\boldsymbol{\sigma}_k = \boldsymbol{Q}_k \boldsymbol{\varepsilon}_k - \boldsymbol{e}_k^T \boldsymbol{E}_k. \tag{2}$$

In equations (1) and (2), $\boldsymbol{\varepsilon}$, $\boldsymbol{\sigma}$, $\boldsymbol{D}$ and $\boldsymbol{E}$ are strain, stress, electric displacement and electric field vectors, and $\boldsymbol{e}$, ε and $\boldsymbol{Q}$ are piezoelectric constants, permittivity coefficients and plane-stress reduced elastic constant matrices, respectively.

2.2 Finite element formulations

A stiffened plate is composed of a plate with a number of shear webs, and the members are assumed to be made up of laminated composites. In this section, a finite element formulation is adopted by using a nine-node plate element with three-node beam elements.

Using the first-order shear deformation plate theory (FSDPT), the displacement fields u, v and w are as follows:
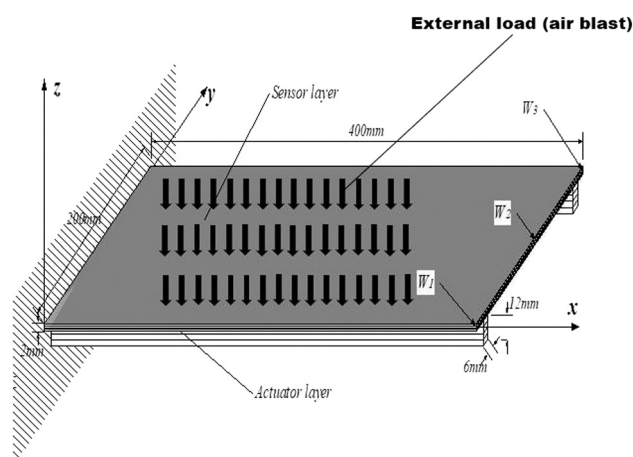
$$u(x, y, z) = u_p^o(x, y) + z\theta_{xp}(x, y)$$
$$v(x, y, z) = v_p^o(x, y) + z\theta_{yp}(x, y) \tag{3}$$
$$w(x, y, z) = w_p^o(x, y, z),$$

where subscript p denotes plate. Furthermore, u_p^o, v_p^o and w_p^o are the midplane displacements, and θ_{px} and θ_{py} are the rotations of transverse normal on x- and y-axis, respectively.

Then, the strain fields of the plate are expressed as a function of the nodal displacement variables, such as

$$\begin{Bmatrix} \varepsilon_{xx} \\ \varepsilon_{yy} \\ \gamma_{xy} \end{Bmatrix}_p = \begin{Bmatrix} u_{p,x}^0 \\ v_{p,y}^0 \\ u_{p,y}^0 + v_{p,x}^0 \end{Bmatrix} + z \begin{Bmatrix} \theta_{px,x} \\ \theta_{py,y} \\ \theta_{px,y} + \theta_{py,x} \end{Bmatrix} \tag{4a}$$

$$= (\boldsymbol{B}_m + z\boldsymbol{B}_b)\boldsymbol{\delta}_p,$$

$$\begin{Bmatrix} \gamma_{xz} \\ \gamma_{yz} \end{Bmatrix}_p = \begin{Bmatrix} w_{p,x}^o - \theta_{px} \\ w_{p,y}^o - \theta_{py} \end{Bmatrix} = \boldsymbol{B}_s\boldsymbol{\delta}_p, \tag{4b}$$

where subscripts m, b, and s denote the membrane strain, bending strain and shear strain, respectively. Furthermore, $\boldsymbol{B}_m$, $\boldsymbol{B}_b$ and $\boldsymbol{B}_s$ are the derivative operators between the strain and nodal displacements, and $\boldsymbol{\delta}_p$ represents the nodal displacement vector of the plate.

The displacement fields for the x-directional shear web can be expressed as follows:

$$u_{sx}(x, z) = u_{sx}^o(x) + z\theta_{sx}(x), \quad w_{sx}(x, z) = w_{sx}^o(x), \tag{5}$$

where subscripts sx denote the x-directional shear webs. In the formulation, the x-axis is taken along the x-directional shear-web centerlines. Furthermore, z-axis is its upward normal line:

$$\boldsymbol{\varepsilon}_{sx} = \boldsymbol{H}_{sx}\boldsymbol{\varepsilon}_{sx}^o = \boldsymbol{H}_{sx}\boldsymbol{B}_{sx}\boldsymbol{\delta}_{sx}, \tag{6}$$

$$\boldsymbol{\sigma}_{sx} = \boldsymbol{Q}_{sx}\boldsymbol{\varepsilon}_{sx}, \tag{7}$$

where $\boldsymbol{\varepsilon}_{sx} = \{\varepsilon_{xx}, 0, 0, \varepsilon_{xz}, 0\}^T$ and $\boldsymbol{\sigma}_{sx} = \{\sigma_{xx}, 0, 0, \tau_{xz}, 0\}^T$.

Additionally, the conditions of displacement compatibility between the plate and the x-directional shear web are given by

$$u_{sx,i}^o = u_{p,i}^o - e_{sx}\theta_{px,i}, \quad \theta_{sx,i} = \theta_{px,i}, \quad w_{sx,i} = w_{p,i}, \tag{8}$$

where $e_{sx} = (t_p/2) + (t_{sx}/2)$. Furthermore, t_p and t_{sx} stand for the plate thickness and the x directional shear-web depth, respectively.

Using a transformation matrix $\boldsymbol{T}_{sx}$, the nodal displacement can be written as $\boldsymbol{\delta}_{sx} = \boldsymbol{T}_{sx}\boldsymbol{\delta}_p$.

Then, applying the extended Hamilton's principle,

$$\int_{t_1}^{t_2} (\delta T - \delta U + \delta W)\mathrm{d}t = 0, \tag{9}$$

where δT and δU are the variation of the total kinetic energy and the total potential energy of the system, respectively, and δW denotes the virtual work of the applied forces.

First, the total kinetic energy is given by

$$T = \sum T^e = \sum \frac{1}{2} \int_{V_{pe}} \rho_p \dot{\boldsymbol{u}}^T \dot{\boldsymbol{u}} \mathrm{d}V + \sum \frac{1}{2} \int_{V_{se}} \rho_s \dot{\boldsymbol{u}}^T \dot{\boldsymbol{u}} \mathrm{d}V, \tag{10}$$

where ρ_p and ρ_s are the mass density of the plate structure with piezoelectric layers and shear web, respectively.

Next, the total potential energy is given by

$$U = \sum U^e = \sum \frac{1}{2} \int_{V_{pe}} \boldsymbol{\varepsilon}_p \boldsymbol{\sigma}_p \mathrm{d}V + \sum \frac{1}{2} \int_{V_{se}} \boldsymbol{\varepsilon}_s \boldsymbol{\sigma}_s \mathrm{d}V. \tag{11}$$

Finally, the work done by external forces is

$$W = \sum W^e = \sum \int_{s_e} \boldsymbol{u}^T \boldsymbol{f}_s \mathrm{d}A, \tag{12}$$

where s_e is the surface area of the plate element with a specified surface force $\boldsymbol{f}_s$.

On the other hand, the electric field vector, $\boldsymbol{E}$, can be expressed as a function of the applied voltage V_a,

$$\boldsymbol{E} = \{0 \quad 0 \quad 1/h_a\}^T V_a = \boldsymbol{B}_v V_a, \tag{13}$$

where h_a is the thickness of the actuator layer.

Substituting equations (10)–(12) into equation (9) and considering the Rayleigh damping, the equation of motion can be obtained as

$$\sum(\boldsymbol{M}_p^e + \boldsymbol{M}_s^e)\ddot{\boldsymbol{\delta}}^e + \sum \boldsymbol{C}^e \dot{\boldsymbol{\delta}}^e + \sum(\boldsymbol{K}_p^e + \boldsymbol{K}_s^e)\boldsymbol{\delta}^e$$
$$= \sum(\boldsymbol{F}^e + \boldsymbol{K}_{av}^e \boldsymbol{V}^e), \tag{14}$$

where

$$\boldsymbol{M}_p^e = \int_V \boldsymbol{N}_p^T \rho_P \boldsymbol{N}_p \mathrm{d}V,$$

$$\boldsymbol{M}_s^e = \int_L \boldsymbol{T}_{xs}^T \boldsymbol{N}_{xs}^T \left(\int_s \boldsymbol{G}_{xs}^T \rho_s \boldsymbol{G}_{xs} \mathrm{d}A \right) \boldsymbol{N}_{xs} \boldsymbol{T}_{xs} \mathrm{d}S,$$

$$\boldsymbol{M}_p^e = \int_A (\boldsymbol{B}_m^T \boldsymbol{A} \boldsymbol{B}_m + \boldsymbol{B}_m^T \boldsymbol{B} \boldsymbol{B}_b + \boldsymbol{B}_b^T \boldsymbol{B} \boldsymbol{B}_m + \boldsymbol{B}_b^T \boldsymbol{D} \boldsymbol{B}_b-$$
$$+ \boldsymbol{B}_s^T \boldsymbol{S} \boldsymbol{B}_s)\mathrm{d}A,$$

$$\boldsymbol{K}_s^e = \int_L \boldsymbol{T}_{xs}^T \boldsymbol{B}_{xs}^T \left(\int_A \boldsymbol{H}_{xs}^T \boldsymbol{Q}_{xs} \boldsymbol{H}_{xs} \mathrm{d}A \right) \boldsymbol{B}_{xs} \boldsymbol{T}_{xs} \mathrm{d}S,$$

$$\boldsymbol{F}^e = \int_A \boldsymbol{N}_p^T \boldsymbol{f}_s \mathrm{d}A,$$

$$\boldsymbol{K}_{av} = \sum_{k=1}^{N_L} (z_{k+1} - z_k) \int_A \boldsymbol{B}_m^T \boldsymbol{e}^T \boldsymbol{B}_V \mathrm{d}A$$
$$+ \frac{1}{2} \sum_{k=1}^{N_L} (z_{k+1}^2 - z_k^2) \int_A \boldsymbol{B}_b^T \boldsymbol{e}^T \boldsymbol{B}_V \mathrm{d}A.$$

Additionally, N_p and N_{xs} are shape function matrices of a plate and a shear web, respectively, G_{xs} is the matrix relating shear web acceleration field to the acceleration vector at the neutral lines A, B, D and S, which are extensional shear web, bending-extension coupling stiffness, bending stiffness and shear stiffness matrix, respectively, and N_L is the number of piezoelectric layers.

The damping matrix C^e is assumed as follows:

$$C^e = \alpha M^e + \beta K^e. \tag{15}$$

Also, a sensor patch is assumed to cover several elements, and the closed circuit charge measured through the electrodes of a sensor patch in the kth layer is

$$q(t) = \sum_{j=1}^{N_s} \frac{1}{2} \left[\int_{S_j(z=z_k)} D_z dA + \int_{S_j(z=z_{k+1})} D_z dA \right], \tag{16}$$

where an electric displacement in the thickness direction D_z is $[e_{31} \ e_{32} \ e_{36}] \varepsilon_p = e_3 \varepsilon_p$, where N_s is the number of elements and S_j is the surface of the jth element.

The sensor voltage is computed as follows:

$$V_s(t) = G_c i(t) = G_c \frac{dq(t)}{dt}, \tag{17}$$

where G_c is the gain of the current amplifier, which transforms the sensor current into voltage. The sensor voltage is fed back into the actuator. Using the constant gain control algorithm, the actuating voltage can be expressed as follows:

$$V_a = G_i V_s = G_i G_c \frac{dq(t)}{dt} = G \sum_{j=1}^{N_s} K_{sv}^j \dot{\delta}, \tag{18}$$

where G_i is the gain to provide a feedback control, and K_{sv} is

$$K_{sv} = \int_A e_3 \left[B_m + \frac{1}{2}(z_k + z_{k+1}) B_b \right] dA. \tag{19}$$

Substituting equation (19) into equation (14) and assembling the element equations gives the global dynamic equation,

$$M\ddot{\delta} + (C - K_{av}GK_{sv})\dot{\delta} + K\delta = F. \tag{20}$$

2.3 Control algorithm

The constant gain negative velocity feedback control algorithm is used as a control algorithm. The formula for element equations of motion is as follows:

$$[M_{uu}]\{\ddot{\delta}_p^e\} + ([K_{uu}] + [K_{u\phi}][K_{\phi\phi}]^{-1}[K_{\phi u}])\{\delta_p^e\}$$
$$= \{F_s^e\} + [K_{u\phi}][K_{\phi\phi}]^{-1}\{F_q^e\}. \tag{21}$$

If the piezoelectric layer is used as an actuator, we have $\{\phi_a^e\} = [K_{\phi\phi}]^{-1}\{F_q^e\}$,

where

$$[M_{uu}]\{\ddot{\delta}_p^e\} + ([K_{uu}] + [K_{u\phi}][K_{\phi\phi}]^{-1}[K_{\phi u}])\{\delta_p^e\}$$
$$= \{F_s^e\} + [K_{u\phi}]\{\phi_a^e\}, \tag{22}$$

In the case of the sensing voltage, $\{\phi_s^e\} = -[K_{\phi\phi}]^{-1}[K_{\phi u}]\{\delta_p^e\}$.

In equation (21), the stiffness matrix term $-[K_{\phi\phi}]^{-1}[K_{\phi u}]\{\delta_p^e\}$ becomes the sensing voltage, while the actuation voltage,

$$\{\phi_a^e\} = -[G]\{\dot{\phi}_s\}$$
$$= -[G](-[K_{\phi\phi}]_{se}^{-1}[K_{\phi u}]_{se}\{\delta_s^e\}) \tag{23}$$
$$= [G][K_{\phi\phi}]_{se}^{-1}[K_{\phi u}]_{se}\{\delta_s^e\}.$$

Finally, the actuating voltage is summarized as $\{\phi_a^e\} = [G][K_{\phi\phi}]_{se}^{-1}[K_{\phi u}]_{se}\{\delta_s^e\}$.

2.4 Shear web location

With regard to the location of a shear web, two stiffeners are placed at the same distance (d) from the centerline along the width of the plate, and the shear-web location can be defined using the following equation:

$$\mu = \frac{d}{C/2}, \tag{24}$$

where μ is the distance between the shear web and the centerline and C is the width of the plate.

Additionally, the displacements are defined as follows [8]:

$$W_L = \frac{W_2}{C}, \ W_T = \frac{W_2 - (W_1 + W_3)/2}{C}, \ W_R = \frac{W_1 - W_3}{C}, \tag{25}$$

where W_L, W_T and W_R are the longitudinal bending, transverse bending and lateral twisting, respectively, and W_1, W_2 and W_3, the lateral deflections at locations, are shown in Figure 2.

2.5 External Load

To study the effects of the piezoelectric actuation and the shear-web location, an external aerodynamic force is applied to the structural model. To simulate the effects of the extreme loading conditions, a blast load is adopted, as shown in Figure 3. It is characterized by an abrupt pressure increase at the shock front, followed by
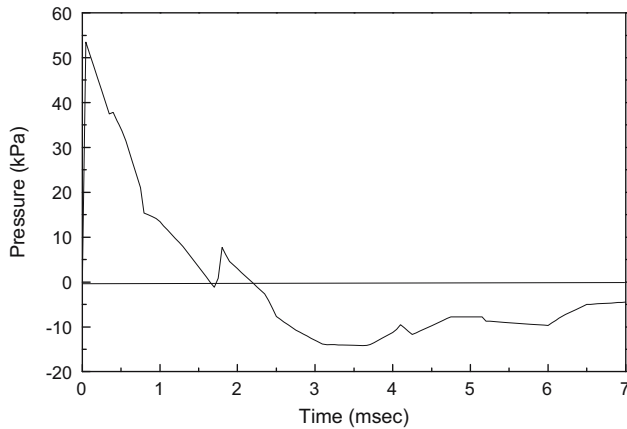
Figure 3: Time variation of average pressure due to air blast on a square plate.

a quasi-exponential decay back to ambient pressure. A negative phase follows, in which the pressure is less than the ambient (p_0), and oscillations between positive and negative overpressures continue as the disturbance quickly disappears. These further oscillations, being of low pressure difference, are not dominant, as compared to the first positive phases, and usually are ignored [27]. Therefore, for simplicity, this variation is ignored and a uniformly distributed pressure is assumed over the entire plate surface.

The variation of the total pressure is given by the Friedlander decay function [28] as

$$P(t)_{\text{blast}} = P_{\text{m}}\left(1 - \frac{t}{t_{\text{p}}}\right)e^{-a't/t_{\text{p}}}, \qquad (26)$$

where P_{m} is a peak pressure, t_{p} is a positive phase duration and a' is the waveform parameter.

3 Numerical simulations and discussion

In this study, a stiffened plate with piezoelectric sensors and actuators subjected to blast loading is considered. The numerical results of the effect of the piezoelectric material and the shear-web location are discussed. The wind turbine blade is replaced by a simplified rectangular model as shown in Figure 2, a cantilever laminated composite plate with two shear webs in the x-direction. The plate is bonded at the upper and lower surfaces by piezomaterials, and two shear webs are installed under the plate to reduce the load. For simplicity, a uniform external load is assumed to be distributed over the

entire plate surface. The upper and lower piezoelectric layers are assumed as sensor and actuators, respectively. The dimension of the plate is 400 mm × 200 mm × 2 mm, and the uniform thickness layer of the plate is $15°/-15°/-15°/15°$. The eccentric shear webs with width 6 mm and depth 12 mm are made up of the same material and consist of four composite layers $(0°/0°/0°/0°)$. The thickness of the piezomaterial layer is 0.2 mm each, and that of the adhesive layers is neglected. Table 1 summarizes the material properties of the composite plate for T300/976 graphite-epoxy and the piezomaterial for PZT-5A [29]. In addition, the air blast load data are used in equation (23), as shown in Figure 3.

As a control algorithm, a constant gain negative velocity feedback control algorithm is used. A modal superposition method is applied in the analysis by considering the first eight modes, and the initial damping ratio for each of the modes is assumed as 0.7%. The Newmark-β direct integration method is used to calculate the transient response of the plate. Due to the implicit integration scheme, a time step size 0.1 ms may be chosen without the loss of numerical stability. In this article, the effects of the shear-web location and control gain for three types of stiffened plates are studied in detail.

3.1 Code verification

To verify the numerical model in this study, the results are compared with the previous data. The first case is a cantilevered laminated composite plate with a size 20 cm × 20 cm, and the total thickness of the plate is 1 mm. The structure consists of four T300/976 graphite-

Table 1: Material properties [29]

Properties	PZT piezomaterial	T300/976
Young's modulus (GPa): E_{11}	63.0	150
$E_{22} = E_{33}$	63.0	9.0
Poisson's ratio: $v_{12} = v_{13}$	0.3	0.3
v_{23}	0.3	0.3
Shear modulus (GPa): $G_{12} = G_{13}$	24.2	7.10
G_{23}	24.2	2.50
Density (kg/m³): ρ	7,600	1,600
Piezoelectric coefficients (pC/N): $d_{31} = d_{32}$	−171	—
d_{33}	374	—
Relative permittivity (ε_r): ε_{33}	1,700	—
Electromechanical coupling factor (k): k_{31}	0.34	—
k_{33}	0.7	—

epoxy composite layers $[-45/45/-45/45]$. Further, the upper and lower surfaces are symmetrically bonded by piezomaterials, PZT-5A, and the two outer piezomaterial layers have a thickness of 0.1 mm each. Also, the thickness of the adhesive layers is assumed to be negligible. These two types of plates are exposed to a uniformly distributed load of 100 N/m², and all the piezomaterials on the upper and the lower surfaces of the plate are used as actuators. Equal amplitude voltages with an opposite sign are applied across the thickness of both piezoelectric layers. The centerline deflections of the composite plate under an input voltage of different actuators are shown in Figure 4. The results are consistent with the data obtained by Lam et al. [30].

As for the second case, the result is the deflection response of a square plate subjected to an air blast. The size of the plate model is 508 mm × 508 mm × 3.4 mm, and its material properties E, v and ρ are 206.84 GPa, 0.3, and 7,900 kg/m³, respectively. The plate is analyzed by a 10 × 10 mesh. The clamped boundary condition is applied on all edges of the plate. The dynamic response is calculated using a mode superposition method, with 18 modes, and the time step is taken as 0.05 ms. Figure 5 shows the results of the present study and the reference data [31,32] for the deflection at the center of the plate during a time interval of 0 to 18 ms. Comparison of the results reveals that the present result shows an acceptable level of difference, as compared to the previous data.

The last case is a glass-reinforced polyester plate with a centrally placed shear web [11]. The two opposite edges are free and the other two edges are clamped. The dimensions of the plate are 300 mm (free) × 375 mm (clamped) × 2.32 mm (thickness) and those of the shear
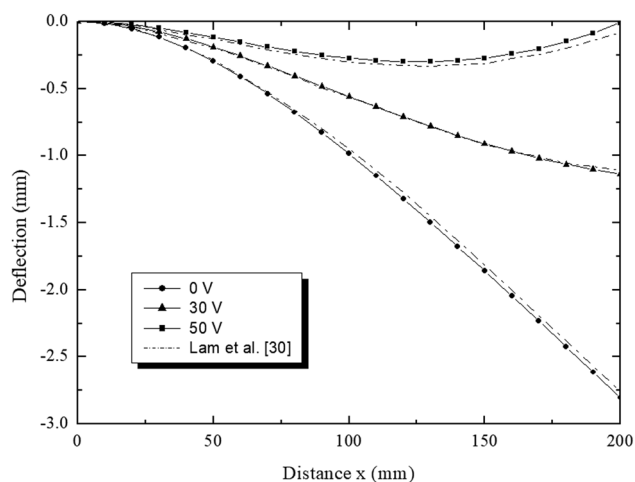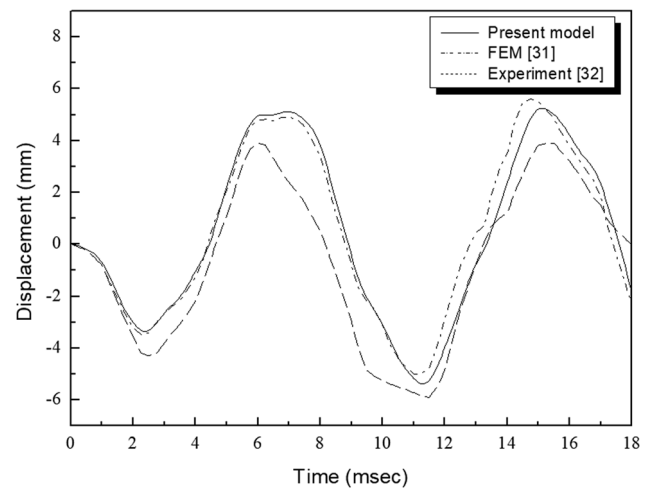
Figure 5: Displacement-time response of the center of the square plate subjected to air blast.

web are 3 mm (width) × 6 mm (depth). The shear web is placed in the centerline of the plate, parallel to the free edges. Both the plate and shear web are made up of the same isotropic material with E = 7.0 GPa, G = 2.6 GPa, ρ = 1504.2 kg/m³ and v = 0.345. The natural frequencies of the system corroborate well with the previous data [11,33], as shown in Table 2.

As shown above, the code used in this calculation corresponds well with the references, and various calculations are performed using this code.

3.2 Vibration suppression of plates with stiffeners under a blast load

The stiffened plate models with three types of shear-web locations are shown in Figure 6. As mentioned in Section 2.3 in detail, various studies were conducted on the behavior of a plate according to the location of the shear web and its control algorithms. In the case of μ = 1, the shear

Figure 4: The centerline deflection under uniform load and different actuator's input voltage.

Table 2: Comparison of natural frequencies (Hz) of stiffened plate

Mode no.	Ref. [11]	Ref. [33]	Present	Discrepancy (%)	
				With Ref. [11]	With Ref. [33]
1st	68.47	68.61	68.13	0.5	0.7
2nd	68.66	71.20	68.77	−0.2	3.5
3rd	119.59	124.70	117.55	1.7	6.1
4th	162.16	150.40	160.12	1.3	−6.1
5th	177.11	183.20	177.45	−0.2	3.2
6th	177.39	184.80	178.31	−0.5	3.6
7th	266.58	251.90	262.58	1.5	−4.1

web is located at the edge of a plate, case 1, as shown in Figure 6(a). On the other hand, in the case of $\mu = 0$, the shear web is located at the center of the plate, case 3, as shown in Figure 6(c). With regard to the location of a shear web, the two stiffeners are placed at the same distance from the centerline, along the width of the plate, as in equation (24 and 25)

3.2.1 Effect of the shear-web locations

The effect of a shear-web location is investigated. Two shear webs are placed at the same distance from the centerline along the width of a plate. In addition, the piezoelectric sensors and actuators are distributed over the entire plate surface. Under these conditions, the

Table 3: Natural frequencies of different shear-web cases

Mode no.	Case 1 ($\mu = 1$)	Case 2 ($\mu = 0.5$)	Case 3 ($\mu = 0$)
1st	67.6	91.4	39.6
2nd	117.7	92.4	78.7
3rd	155.3	205.2	133.6
4th	212.1	294.7	178.3
5th	290.4	337.2	214.4
6th	379.4	450.2	273.3

modal analysis is performed and the results are shown in Table 3, which lists the first six natural frequencies of the stiffened plate under different cases: case 1 ($\mu = 1$), case 2 ($\mu = 0.5$) and case 3 ($\mu = 0$). It reveals that the natural frequencies of case 2 are higher than those of other cases, except for the second mode. Additionally,
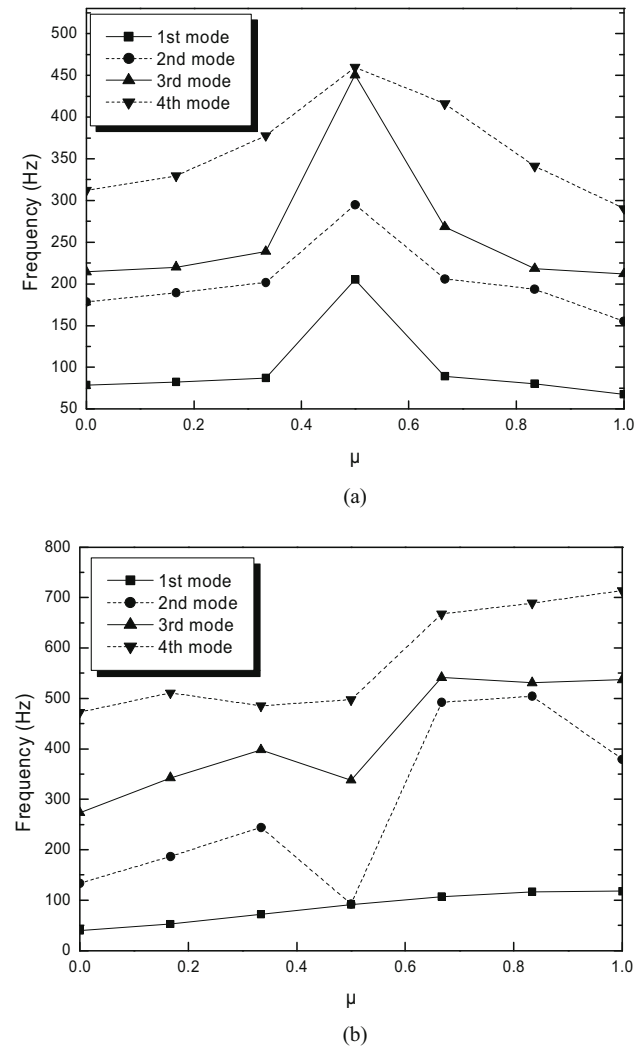

Figure 6: Three cases of shear-web location: (a) case 1, (b) case 2 and (c) case 3.

Figure 7: Natural frequencies for different shear-web locations: (a) bending modes and (b) twisting modes.

the results of the natural frequencies of the stiffened plate under different shear-web locations (μ) are shown in Figure 7. It can be seen from Figure 7(a) that the natural frequencies of the bending mode at $0.4 \leq \mu \leq 0.6$ are higher than those of others. Moreover, the natural frequencies of the twisting mode at $0.8 \leq \mu \leq 1$ are higher than those of others, as shown in Figure 7(b). Therefore, the stiffened plates, of which the shear webs are placed at the centerline or free edge, are more flexible for the bending mode. When the shear webs are placed between the centerline and the free edge, the stiffness of the stiffened plates is increased for the bending mode. However, the stiffness of a twisting mode is increased at the free edge. Accordingly, the shear-web locations have an effect on the stiffness of the stiffened plate.
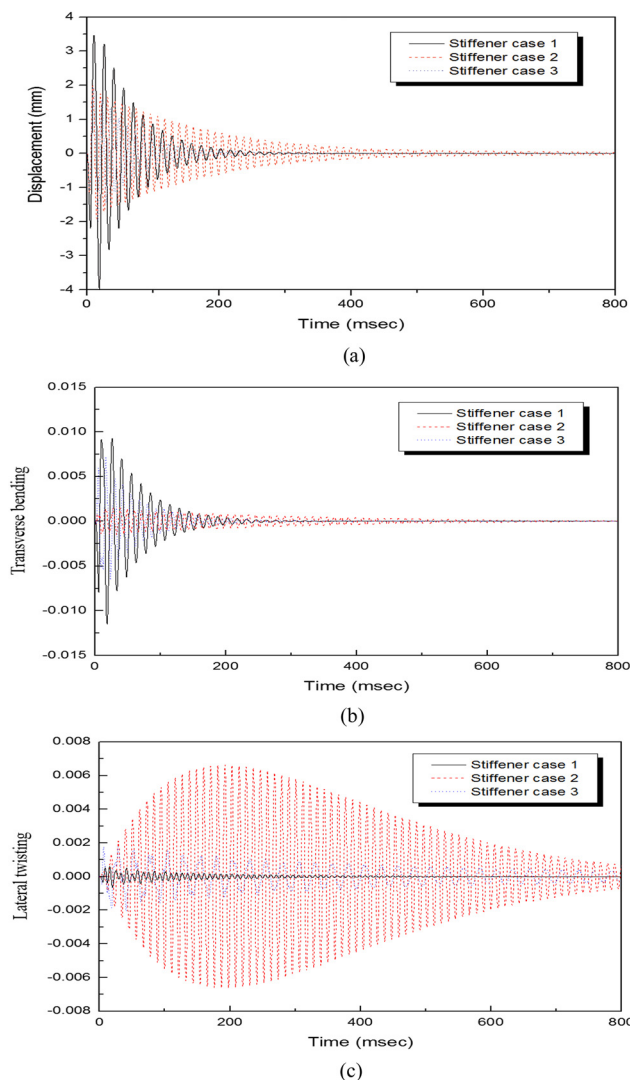
In addition, at a specific constant gain ($G = 3,000$), the response comparison such as vertical displacement, transverse bending and lateral twisting with three shear-web cases are shown in Figure 8. The controlled displacements of the shear-web case 1 are damped out more effectively when compared to the shear-web cases 2 and 3; however, a peak vertical displacement appeared in the shear-web case 1. Moreover, the transverse bending of the shear-web cases 1, 2 and 3 show the same tendency as with the vertical displacement; however, an effective vibration control can be performed for the shear-web case 2. The lateral twisting of the shear-web case 1 is most effective, as compared to other cases. Therefore, when determining the optimum shear-web position, considering the characteristics of the load direction acting on the wind turbine blades is more important.
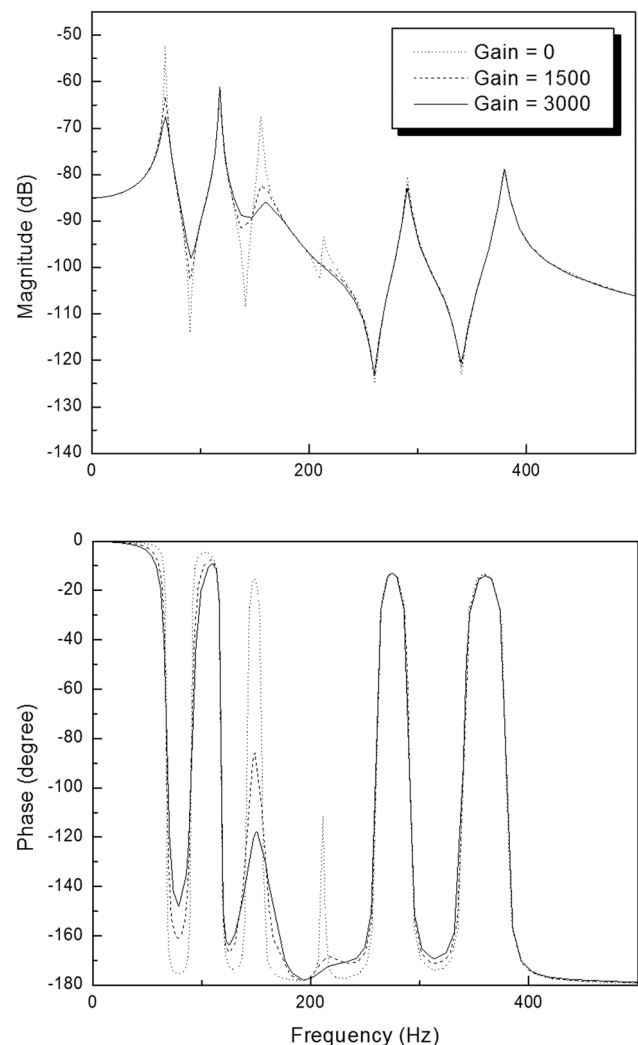

Figure 8: Response comparison of the three shear-web cases (gain = 3,000): (a) vertical displacement, (b) transverse bending and (c) lateral twisting.

Figure 9: Frequency response of the shear-web case 1 due to a different feedback control gain.

3.2.2 Effect of a control gain

To investigate the effect of a control gain with various shear-web locations on control performance, typical configurations (μ = 0, 0.5 and 1) of the stiffened plate are considered in this study. Figures 9, 11 and 13 show the frequency responses for each stiffener's locations, using the constant gain negative velocity feedback control law. The curves of the deflection magnitude of the unit input force applied at the tip point and frequency due to different feedback control gains are investigated. The responses of the plates are calculated at the same location. Figure 9 shows a frequency response of the stiffened plate ($\mu = 1$) due to different feedback control gains. The figure shows that the controlled responses have a lower magnitude of the first, second and third bending modes. The vertical displacement at the tip, transverse bending and lateral twisting for various control gains, when a stiffened plate is subjected to a uniformly distributed air blast pressure, are given in Figure 10. It can be seen that the vibration of a stiffened plate with a higher control gain is damped out more quickly.

In the case of $\mu = 0.5$, the frequency responses are shown in Figures 11 and 12 shows the vertical displacement at the tip, transverse bending and lateral twisting for various control gains. The controlled responses have a lower magnitude of first and second bending modes. However, Figures 13 and 14 show that the effect of a control gain is weaker than the other stiffener's locations, and the vibration of a lateral twisting has a higher magnitude than those of others. This may be due to an increased stiffness
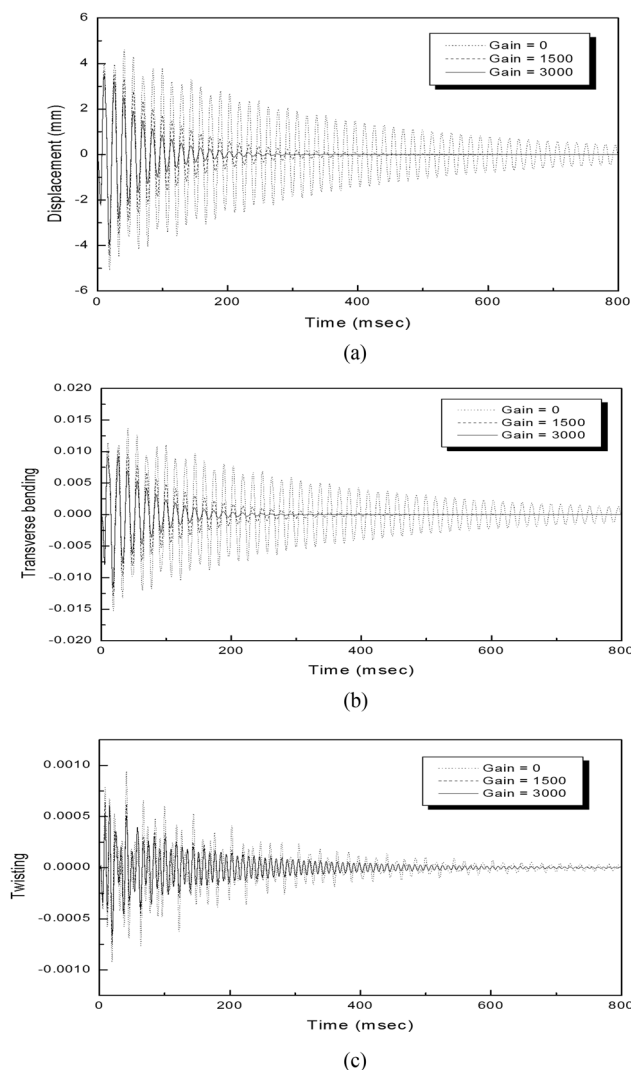

Figure 10: Responses of a stiffened plate (case 1) with various control gains: (a) vertical displacement, (b) transverse bending displacement and (c) lateral twisting displacement.
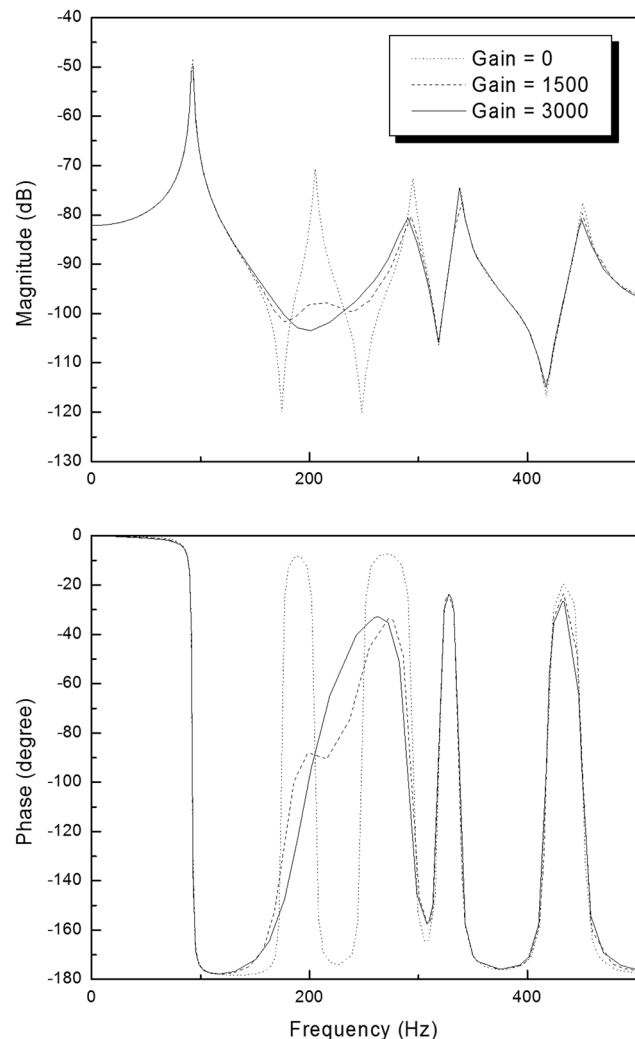

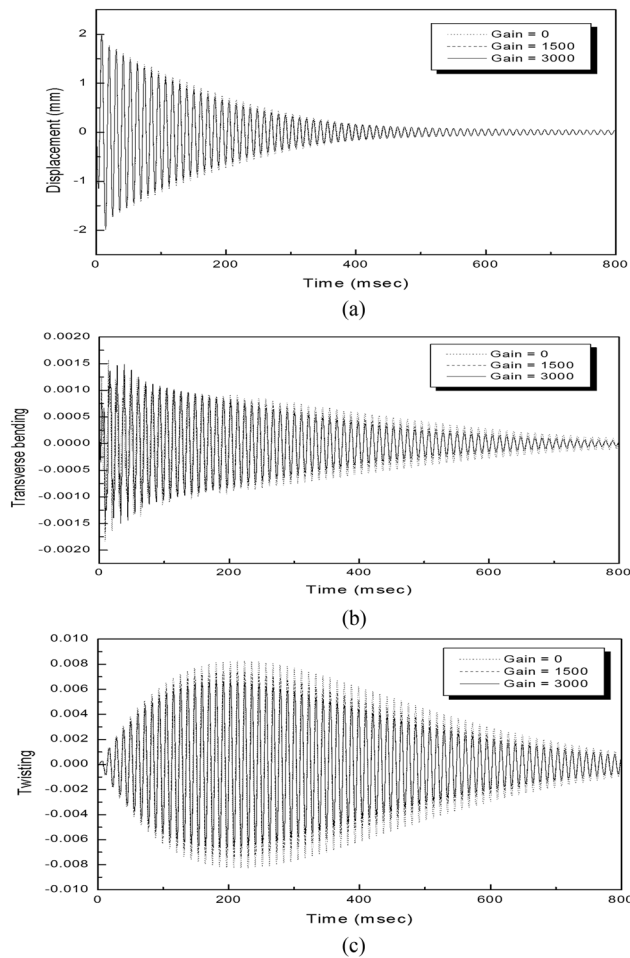**Figure 11:** Frequency response of the shear-web case 2 due to a different feedback control gain.

Figure 12: Responses of a stiffened plate (case 2) with various control gains: (a) vertical displacement, (b) transverse bending displacement and (c) lateral twisting displacement.

Figure 13: Frequency response of the shear-web case 3 due to a different feedback control gain.

associated with the stiffener's location. Considering the stiffener's location in the case of $\mu = 0$, it can be seen that the lower magnitude of first, second and third bending modes for higher control gains and the vibration is damped out more quickly, except for the lateral twisting.

As can be seen from Figures 9–14, the piezoelectric actuators can control the bending modes effectively; however, the control of the torsion modes is weak in the cases of all the stiffeners. This indicates that the vibration amplitude decays depend on the modal damping and the feedback control gain. According to equation (17), increasing the feedback control gains can result in a higher damping matrix in the system equation. Therefore, the vibration of a plate can be suppressed much faster at higher feedback control gains. It is important to optimize the control algorithm with the location of the shear web by considering the characteristics of the load direction applied to the wind turbine blades.
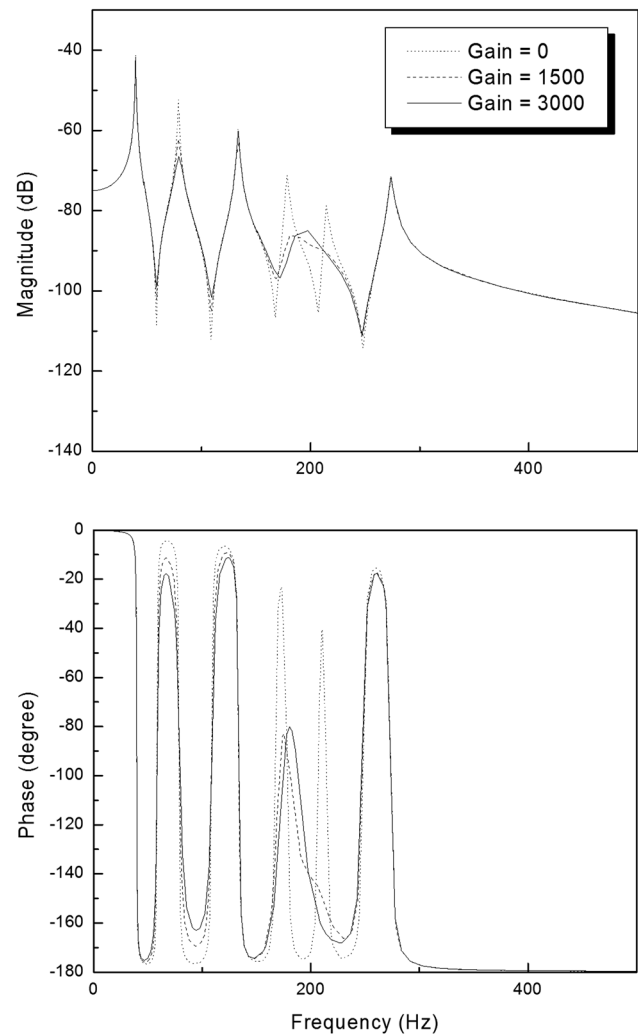
4 Conclusion

This article presents a transient response of a stiffened plate with the piezoelectric sensors and actuators subjected to external wind loads. The formulation is based on the first-order shear deformation theory of plate and beam. The constant negative velocity feedback control algorithm is used as a control scheme. The external wind load is assumed to be uniformly distributed on the plate surface. The numerical model is validated with theoretical and experimental data from the literature. In this study, the vibration characteristics and transient responses are compared with control algorithms and various shear-web locations.

When the piezoelectric patches are distributed over the entire surface of a plate, the effect of a shear-web location is investigated with three types of typical
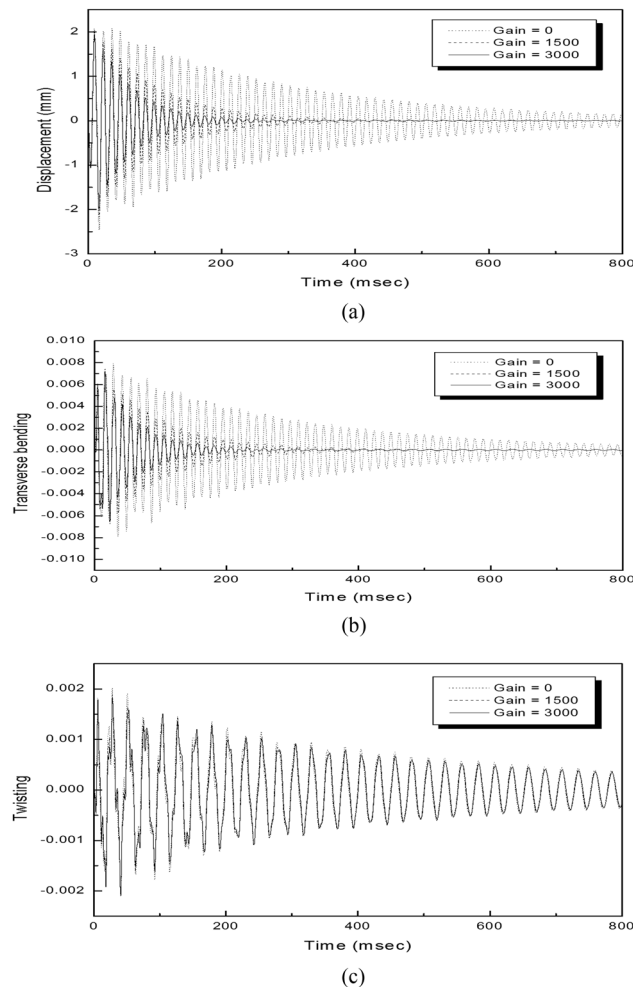
Figure 14: Responses of a stiffened plate (case 3) with various control gains: (a) vertical displacement, (b) transverse bending displacement and (c) lateral twisting displacement.

configurations. The shear-web locations have an effect on the stiffness of the stiffened plate. When the shear webs are placed between the centerline and the free edge, the stiffness of the stiffened plates is increased for a bending mode. However, the stiffness of a twisting mode is increased at free edges. Using a negative velocity feedback control algorithm, the control effect of a shear-web location at the middle of a plate (case 2) is weaker than those of others because of the increased stiffness due to the shear-web location. Moreover, the piezoelectric actuators can control the bending modes effectively; however, the control of the torsion modes is weak in all shear-web cases.

Therefore, optimizing the shear-web position and control algorithm according to the various load directions applied to the wind turbine blade is important. In the future, as an extension of the active vibration suppression method proposed in this article, an improved control algorithm will apply to the wind turbine blade for a load reduction.

Conflict of interest: Author states no conflict of interest.

References

[1]   Song ZG, Li FM. Active aeroelastic flutter analysis and vibration control of supersonic composite laminated plate. Comp Struct. 2012;94:702–13.
[2]   Qiao YH, Han J, Zhang CY, Chen J. Active vibration control of wind turbine blades by piezoelectric materials. Chin J Appl Mech. 2013;30(4):587–92.
[3]   Chandiramani NK. Active control of a piezo-composite rotating beam using coupled plant dynamics. J Sound Vib. 2010;329:2716–37.
[4]   Li FM. Active aeroelastic flutter suppression of a supersonic plate with piezoelectric material. Int J Mech Sci. 2012;51:190–203.
[5]   Kapuria S, Yasin MY. Active vibration suppression of multi-layered plates integrated with piezoelectric fiber reinforced composites using an efficient finite element mode. J Sound Vib. 2010;329:3247–65.
[6]   Phung PV, Lorenzis LD, Chien HT, Wahab MA. Analysis of laminated composite plates integrated with piezoelectric sensors and actuators using higher-order shear deformation theory and isogeometric finite elements. Comput Mater Sci. 2015;96:495–550.
[7]   Arefi M, Zenkour AM. Vibration and bending analysis of a sandwich microbeam with two integrated piezo-magnetic face-sheets. Comp Struct. 2017;159(1):479–90.
[8]   Arefi M, Zenkour AM. Size-dependent vibration and bending analyses of the piezomagnetic three-layer nanobeams. Appl Phys A. 2017;123:202.
[9]   St-Amant Y, Cheng L. Simulations and experiments on active vibration control of a plate with integrated piezoceramics. Thin-Walled Struct. 2000;38(2):105–23.
[10] Balamurugan V, Narayanan S. Shell finite element for smart piezoelectric composite plate/shell structures and its application to the study of active vibration control. Finite Elem Anal Des. 2001;37(9):713–38.
[11] Mukherjee A, Joshi SP, Ganguli A. Active vibration control of piezolaminated stiffened plates. Comp Struct. 2002;55(4):435–43.
[12] Sadek EA, Tawfik SA. A finite element model for the analysis of stiffened laminated plates. Comput Structure. 2000;75(4):369–83.
[13] Song ZG, Li FM. Aerothermoelastic analysis and active flutter control of supersonic composite laminated cylindrical shells. Comp Struct. 2013;106:653–60.

[14] Shen SH, Yang DQ. Nonlinear vibration of anisotropic laminated cylindrical shells with piezoelectric fiber reinforced composite actuators. Ocean Eng. 2014;80:36–49.

[15] Mirzaei MMH, Arefi M, Loghman A. Creep analysis of a rotating functionally graded simple blade: steady state analysis. Steel Comp Struct. 2019;33(3):463–72.

[16] Mirzaei MMH, Arefi M, Loghman A. Thermoelastic analysis of a functionally graded simple blade using first-order shear deformation theory. Mech Adv Comp Structure. 2020;7(1):147–55.

[17] Mirzaei MMH, Loghman A, Arefi M. Time-dependent creep analysis of a functionally graded beam with trapezoidal cross section using first-order shear deformation theory. Steel Comp Struct. 2019;30(6):567–76.

[18] Arefi M, Zenkour AM. Size-dependent electro-elastic analysis of a sandwich microbeam based on higher-order sinusoidal shear deformation theory and strain gradient theory. J Intell Mater Syst Struct. 2018;29(7):1394–1406.

[19] Arefi M, Zenkour AM. Transient analysis of a three-layer microbeam subjected to electric potential. Int J Smart Nano Mater. 2017;8(1):20–40.

[20] Kiani Y. Torsional vibration of functionally graded carbon nanotube reinforced conical shells. Sci Eng Comp Mater. 2016;July 21:41–52.

[21] Jalaei MH, Civalek O. On dynamic instability of magnetically embedded viscoelastic porous FG nanobeam. Int J Eng Sci. 2019;143:14–32.

[22] Demir C, Civalek O. On the analysis of microbeams. Int J Eng Sci. 2017;121:14–33.

[23] Ebrahimi F, Barati MR, Civalek O. Application of Chebyshev-Ritz method for static stability and vibration analysis of non-local microstructure-dependent nanostructures. Eng Computers. 2020;36:953–64.

[24] Liu T. Classical flutter and active control of wind turbine blade based on piezoelectric actuation. Shock Vib. 2015;2015:13. Article ID 292368, 13 pages.

[25] Abdelrahman WG, Al-Garni AZ, Abdelmaksoud SI, Abdallah A. Effect of Piezoelectric Patch Size and Material on Active Vibration Control of Wind Turbine Blades. J Vib Eng Technol. 2018;6:155–61.

[26] Hulskamp AW, Wingerden JW, Barlas T, Champliaud H, van Kuik GAM, Bersee HEN, et al. Design of a scaled wind turbine with a smart rotor for dynamic load control experiments. Wind Energy. 2011;14:339–54.

[27] Jacinto AC, Ambrosini RK, Danesi RF. Experimental and computational analysis of plates under air blast loading. Int J Impact Eng. 2001; 25(10):927–47.

[28] Gupta AD, Gregory FH, Bitting RL, Bhattacharya S. Dynamic analysis of an explosively loaded hinged rectangular plate. Comput Struct. 1987;26(1–2):339–44.

[29] Uchino K. "Future of ferroelectric devices", ferroelectric devices. 2nd ed. Boca Raton: CRC Press; 2009. p. 297–338.

[30] Lam KY, Peng XQ, Liu1 GR, Reddy JN. A finite-element model for piezoelectric composite laminates. Smart Mater Struct. 1997;6(5):583–91.

[31] Mukherjee A. On finite element dynamic and stability analyses of stiffened plate structures. PhD Thesis. Kharagpur, India: Department of Naval Architecture, IIT Kharagpur; 1987.

[32] Houlston R, Slater JE, Pegg N, Desrochers CG. On analysis of structural response of ship panels subjected to air blast loading. Comput Struct. 1985;21:273–89.

[33] Attaf B, Hollaway L. Vibrational analyses of stiffened and unstiffened composite plates subjected to in-plane loads. Composites. 1990;21(2):117–26.